Draelos-Hagerty, L., Nandwana, P. and Srivastava, A., 2023. Microscale drivers and mechanisms of fracture in post-processed additively manufactured Ti–6Al–4V. International Journal of Fracture, 242(2), pp.207-225.

Microscale drivers and mechanisms of fracture in post-processed additively manufactured

Ti-6Al-4V

Lara Draelos-Hagerty<sup>1</sup>, Peeyush Nandwana<sup>2</sup>, Ankit Srivastava<sup>1,\*</sup>

<sup>1</sup>Department of Materials Science & Engineering, Texas A&M University, College Station, TX 77843, USA

<sup>2</sup>Materials Science and Technology Division, Oak Ridge National Laboratory, Knoxville, TN 37932, USA

## **Abstract**

Herein, we focus on understanding the microstructure-fracture correlations in a Ti-6Al-4V alloy additively manufactured via electron beam melting (EBM) and subjected to various post-process heat-treatments. Specifically, the as fabricated material is subjected to one sub-transus heattreatment followed by air-cooling and two super-transus heat-treatments followed by either air- or furnace-cooling. Next, a series of in-situ single edge notch tension (SENT) tests are carried out under a high-resolution digital optical microscope. The panoramic high-resolution images captured during the in-situ tests are then used to characterize the planar deformation on the specimen surface using microstructure-based digital image correlation (DIC). The results of the in-situ SENT tests together with DIC and post-mortem fractographic analyses provided us with a better understanding of the microstructure-fracture correlations in these materials. Our results show that the fracture mechanism of the as fabricated and sub-transus heat-treated materials is essentially the same, while the changes in the microstructure following the super-transus heattreatments significantly affects the fracture mechanism. In this case, several microcracks of hundreds of microns in length first nucleate away from the deformed notch following extreme plastic deformation at discrete locations. Furthermore, the location of these microcracks in the super-transus heat-treated materials is extremely sensitive to the details of the underlying microstructure.

Tel.: +1 979 458 9841; E-mail: ankit.sri@tamu.edu

<sup>\*</sup>Corresponding Author.

**Keywords:** Additive manufacturing; Titanium alloys; In-situ fracture test; Digital image correlation; Crack nucleation; Fracture Mechanism

## 1. Introduction

A layer-by-layer additive manufacturing using the electron beam (EBM) process exposes a material to a complex thermal cycle wherein the individual layers are preheated, melted, rapidly solidified and partially re-melted multiple times (Murr et al., 2012, Frazier, 2014, Herzog et al., 2016, Liu and Shin, 2019). This complex thermal cycle leads to microstructures and textures in material systems such as Ti-6Al-4V that are unique to the EBM process. The microstructure of EBM processed Ti-6Al-4V comprises basketweave  $\alpha$ -phase morphology within large columnar prior  $\beta$ -phase grains with a  $\langle 001 \rangle$  fiber texture along the build direction, and a continuous  $\alpha$ -phase along the prior  $\beta$ -phase grains (Al-Bermani et al., 2010, Zhai et al., 2015, Galarraga et al., 2017, Nandwana et al., 2019, Kok et al., 2018, Antonysamy et al., 2013, de Formanoir et al., 2016, Murr et al., 2009, Facchini et al., 2009, Draelos et al., 2020, Zhao et al., 2016). The additively manufactured materials are also sometimes subjected to post-process treatments such as hot isostatic pressing (HIP) to eliminate process and feedstock-induced defects. During HIP, it is the associated heat-treatment that mainly affects the material microstructure (Cunningham et al., 2017, Tammas-Williams et al., 2015, Nandwana et al., 2019) and can be carried out above (de Formanoir et al., 2016, Galarraga et al., 2017) or below (Al-Bermani et al., 2010, Raisson and Samarov, 1996, Galarraga et al., 2017) the  $\beta$ -transus temperature (~995°C).

A heat-treatment of the EBM processed Ti-6Al-4V below the  $\beta$ -transus temperature (sub-transus) preserves the columnar grain morphology and initial texture and leads to coarsening of the  $\alpha$ -phase. This in turn decreases both the yield and tensile strengths without significantly affecting the ductility of the material (de Formanoir et al., 2016, Draelos et al., 2020, Nandwana et al., 2019). On the other hand, a heat-treatment above the  $\beta$ -transus temperature (super-transus) transforms the columnar prior  $\beta$ -phase grains into an equiaxed morphology with multiple colonies of similarly oriented  $\alpha$ -phase lamellae within each grain (Draelos et al., 2020, Nandwana et al., 2019, de Formanoir et al., 2016, Galarraga et al., 2017). The size of the microstructural features such as  $\alpha$ -phase lamellae, colonies, and grain boundary  $\alpha$ -phase depends on the cooling rate post super-

transus heat-treatment with higher cooling rate resulting in finer features. The size of the prior  $\beta$ phase grains, on the other hand, predominantly depends on the peak temperature and hold time at
the peak temperature. The strength levels of the super-transus heat-treated materials can be greater
than the sub-transus heat-treated materials but with lower ductility (Draelos et al., 2020).
Following this, the objective of this work is to understand how the different hierarchy of
microstructural features within these materials affect their fracture response.

The microstructure-fracture correlation of both additively (Book and Sangid, 2016, Ren et al., 2017, de Formanoir et al., 2016, Liu et al., 2021, Draelos et al., 2020) and conventionally (Jha et al., 2021, Cvijović-Alagić et al., 2014, Dang et al., 2019, Lutjering and Williams, 2007) manufactured Ti-6Al-4V has been analyzed in the past using post-mortem analyses of the fractured specimens and limited in-situ analysis of tensile dog-bone specimens. These works have shown that depending on the microstructure, fracture in Ti-6Al-4V can initiate at the grain boundary  $\alpha$ phase, boundaries of the colonies of  $\alpha$ -phase lamellae,  $\alpha/\beta$  interface and/or within the  $\alpha$ -phase. However, oftentimes even for the same microstructure-type different fracture initiation sites have been either observed or postulated. For example, in microstructures with basketweave  $\alpha$ -phase morphology within prior  $\beta$ -phase grains, strain localization has been observed in the prior  $\beta$ -phase grains (Book and Sangid, 2016) and microcracking has been observed near the grain boundaries (Ren et al., 2017). Similarly, in microstructures with colonies of  $\alpha$ -phase lamellae within prior  $\beta$ phase grains, fracture initiation has been postulated to occur either preferentially within  $\alpha$ -phase lamella, at the prior  $\beta$ -phase grain boundaries or at the boundaries of the colonies of  $\alpha$ -phase lamellae (de Formanoir et al., 2016). The difference in the fracture initiation site between the two microstructure-types is rather easy to apprehend but the variations in the fracture initiation sites within the same microstructure-type is not a priori obvious. Furthermore, this leads to a more fundamental question: are these changes in the fracture initiation sites also accompanied by changes in the micro-mechanisms?

Herein, we focus on understanding the microscale drivers and mechanisms of fracture in an EBM processed Ti-6Al-4V subjected to various post-process heat-treatments. Specifically, the as fabricated material is subjected to three heat-treatments, one sub-transus heat-treatment (at 920°C) followed by air-cooling and two super-transus heat-treatments (at 1100°C) followed by either air-

or furnace-cooling. This gives us two microstructure-types: one with columnar prior  $\beta$ -phase grains comprising basketweave  $\alpha$ -phase microstructure and intergranular  $\alpha$ -phase, and second with equiaxed prior  $\beta$ -phase grains comprising colonies of  $\alpha$ -phase lamellae microstructure and intergranular  $\alpha$ -phase. Next, in-situ single edge notch tensile (SENT) tests of the as fabricated and three post-process heat-treated material are carried out under a high-resolution digital optical microscope. Although the presence of an initial notch in the specimens leads to extremely large local deformations making it challenging to carry out in-situ experiments, it somewhat guarantees that the focus of the in-situ experiment and the location of the maximum action are the same which is not the case with in-situ experiments involving flat dog-bone specimens. Furthermore, often during in-situ experiments there is a trade-off between the field of view and the resolution; the use of a high-resolution optical microscope capable of panoramic imaging allows us to capture large areas without sacrificing resolution to visualize real-time microstructural changes. These panoramic high-resolution images are then used to characterize the planar deformation utilizing two-dimensional microstructure-based digital image correlation (DIC) to the extent possible. The results of the in-situ SENT tests together with microstructure-based DIC and post-mortem fractographic analyses allow us to better understand how the different hierarchy of microstructural features within the as fabricated and post-process heat-treated Ti-6Al-4V affect their fracture response.

### 2. Material and methods

An Arcam Q10 EBM system at Oak Ridge National Laboratory's Manufacturing Demonstration Facility was used to fabricate all Ti-6Al-4V samples considered in this work. The samples were fabricated using pre-alloyed atomized Ti-6Al-4V powder and standard Arcam processing parameters (Nandwana et al., 2019, Galarraga et al., 2016, Galarraga et al., 2017). The nominal composition (in wt%) of the powders used was 5.82 Al, 4.23 V, 0.141 O, 0.2 Fe, and balance Ti.

The as fabricated material was subjected to three post-process heat-treatments in a tube furnace under Argon atmosphere. The heat-treatments carried out were as follows: a sub-transus heat-treatment at 920°C for 1hr followed by air-cooling (AC) and super-transus heat-treatments at

1100°C for 1hr followed by either air- or furnace-cooling (FC). Henceforth, these heat-treatments are referred to as 920AC, 1100AC and 1100FC.

Next, sub-sized flat SENT specimens from all heat-treated materials as well as the as fabricated material were machined using electrical discharge machining with tensile axis parallel to the initial build direction. The length, width, and thickness of the gauge section of the specimens were 8mm, 3mm and 1mm, respectively. In all the specimens a 1.5mm long notch was introduced in the middle of the gauge section using a wire saw equipped with  $80\mu m$  diameter diamond wire. Although the objective of this work is not to measure standard mechanical properties, but to understand the microscale drivers and mechanisms of fracture in an EBM processed Ti-6Al-4V, we do, however, note that the aspect ratios of the sub-sized single-edge notch specimens are in compliance with the British standard (BS:8571, 2018). The SENT tests were carried out at a (far field) nominal tensile strain rate of  $0.5 \times 10^{-3} \text{sec}^{-1}$  using a Kammrath & Weiss miniaturized tension module under a high-resolution Olympus DSX 510 digital optical microscope.

Two sets of SENT specimens were used for the tests: (i) as-machined (unpolished) specimens, and (ii) specimens with one surface mechanically polished and chemically etched. The polishing procedure was as follows: grinding using 320grit SiC paper followed by rough polishing with 9μm diamond paste and fine polishing using a solution of 1 part 30% H<sub>2</sub>O<sub>2</sub> combined with 3 parts 0.02μm colloidal silica suspension. The polished surfaces were then chemically etched with Kroll's reagent (100ml H<sub>2</sub>O, 2ml HF, 4ml HNO<sub>3</sub>) for 5-20sec to reveal the microstructure. The microstructure on the polished surfaces (before chemical etching) was characterized using backscattered electron (BSE) imaging in a Phenom XL scanning electron microscope (SEM).

All the in-situ tests of polished and etched SENT specimens were interrupted at regular intervals to capture a series of large-scale panoramic images with microstructural-scale resolution. Specifically, a  $2500\times2500~\mu\text{m}^2$  area of interest centered around the notch-tip was imaged by stitching together four images of microstructural-scale resolution with an overlap of ~10%. The in-situ tests with unpolished unetched SENT specimens were carried out uninterrupted and a video of the deforming notch was captured. The fracture surfaces as well as the deformed surfaces of the

fractured specimens below the fracture surface were also imaged using Secondary electron (SE) imaging in a Phenom XL SEM.

The series of panoramic high-resolution images of the surface microstructure captured during the in-situ tests were then used to carry out microstructure-based DIC. This procedure utilizes microstructural features as correlation points (Kang et al., 2007, Ososkov et al., 2007, Han et al., 2013, Marteau et al., 2013, Tasan et al., 2014, Zheng et al., 2020, Draelos et al., 2020). The DIC analysis was performed using an open-source DIC software, Ncorr (Blaber et al., 2015). Ncorr employs a subset-based algorithm where the reference image is partitioned into smaller regions referred to as subsets. These subsets start as a circular group of contiguous points and change shape based on pixel movement. Since the microstructure near the notch tip underwent extremely high deformation, the high strain DIC analysis was used to estimate Euler-Almansi strain tensor. The high strain DIC analysis procedure uses a continuously updated reference image, in which the previous image is used as the reference image as opposed to a fixed reference image.

### 3. Results

### 3.1 Material microstructure

The BSE-SEM images of the as fabricated and all post-process heat-treated microstructures along the build direction are shown in Fig. 1. In the BSE images, the aluminum rich  $\alpha$ -phase appears dark-colored, varying in shades of gray, while the vanadium rich  $\beta$ -phase appears light-colored. The microstructure of the EBM processed (as fabricated) material consists of columnar prior  $\beta$ -phase grains along the build direction with  $\beta$ -phase ribs separating  $\alpha$ -phase laths and continuous  $\alpha$ -phase layer along the grain boundaries, Fig. 1(a). This microstructure, known as basketweave, is typical of EBM processed Ti-6Al-4V. In Fig. 1(b), the basketweave  $\alpha$  morphology within the columnar prior  $\beta$ -phase grains are maintained, albeit coarsened, resulting from the sub-transus heat-treatment of the as fabricated material.

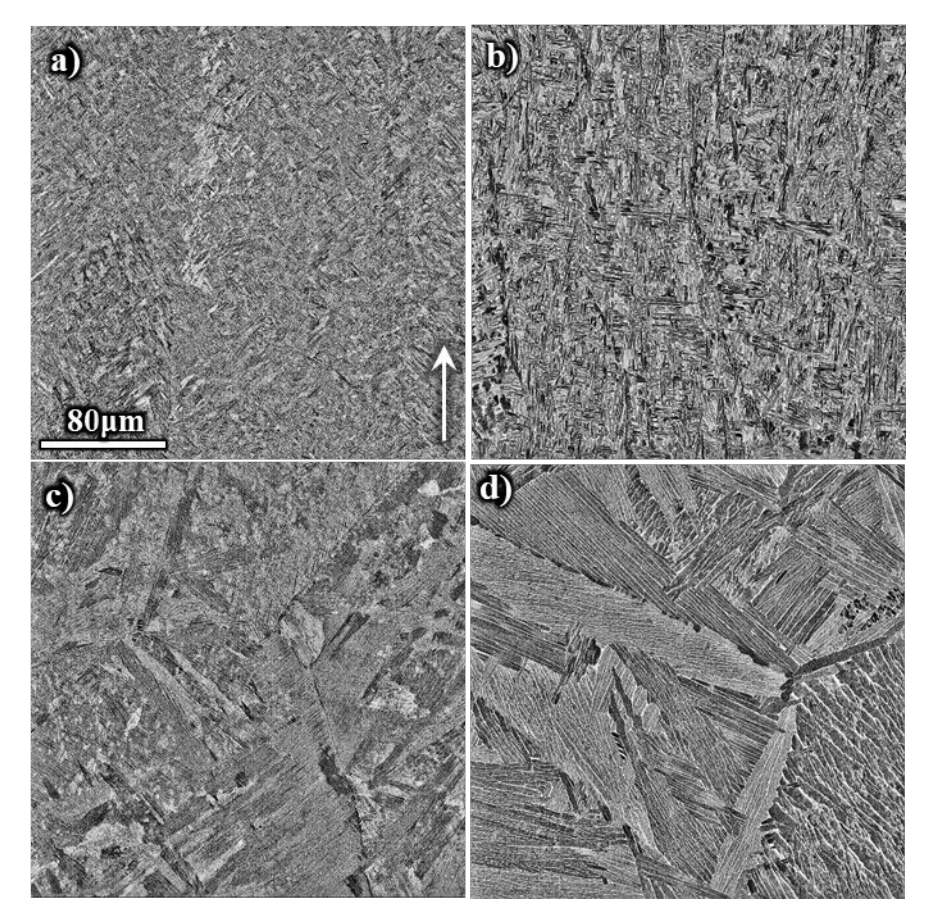


**Figure 1:** BSE-SEM images of the microstructures of **(a)** as fabricated, **(b)** 920°C/1hr/air-cooled (920AC), **(c)** 1100°C/1hr/air-cooled (1100AC) and **(d)** 1100°C/1hr/furnace-cooled (1100FC) materials. In the BSE images, the darker regions are  $\alpha$ -phase while the lighter regions are  $\beta$ -phase. The arrow in (a) marks the build direction and the scale bar is consistent in (a)-(d).

The super-transus post-process heat-treatments of the as fabricated EBM processed Ti-6Al-4V resulted in a transformation of the prior  $\beta$ -phase grains from columnar to equiaxed morphology, as can be seen for 1100AC and 1100FC materials in Figs. 1(c) and (d), respectively. Additionally, the  $\alpha$ -phase transformed from a basketweave morphology to a lamellar morphology, in which a single grain consists of several colonies of  $\alpha$ -phase lamellae and a continuous  $\alpha$ -phase layer along the prior  $\beta$ -phase grain boundaries. The size of the colonies of the  $\alpha$ -phase lamellae as well as the thickness of the  $\alpha$ -phase laths within the colonies depend on the cooling rate from the super-transus heat-treatment temperature, such that they decrease with increasing cooling rate.

The sizes of relevant microstructural features, such as the thickness of the  $\alpha$ -phase laths in the asfabricated materials and three post-process heat-treated materials, as well as the sizes of the colonies of the  $\alpha$ -phase lamellae in the 1100AC and 1100FC materials, were also characterized using multiple BSE-SEM images of the microstructures and a procedure similar to the Heyn linear intercept procedure (ASTM:E112-13, 2013). The cumulative distribution function (CDF) of the thickness of the  $\alpha$ -phase laths and the size of the colonies of the  $\alpha$ -phase lamellae is shown in Figs. 2(a) and (b), respectively. The CDF curves represent the cumulative probability of the size being less than or equal to a given value on the x-axis. As shown in Fig. 2(a), subjecting the material to a sub-transus heat-treatment leads to an increase in the thickness of the  $\alpha$ -phase laths. Specifically, the  $\alpha$ -phase lath thicknesses are  $0.7\pm0.2\mu m$  and  $1.4\pm0.3\mu m$  in the as fabricated and 920AC microstructures, respectively. Moreover, in the super-transus heat-treated materials, the thicknesses of the  $\alpha$ -phase laths are greater in the 1100AC materials compared to the 1100FC materials. The estimated thicknesses of the  $\alpha$ -phase laths in the 1100AC and 1100FC microstructures are  $0.9\pm0.3\mu m$  and  $2.4\pm0.4\mu m$ , respectively. Similarly, in the super-transus heat-treated materials, the sizes of the colonies of  $\alpha$ -phase lamellae are greater in the 1100FC materials compared to the 1100AC materials. In 1100AC and 1100FC materials, the estimated sizes of the colonies of  $\alpha$ -phase lamellae are greater in the 2.5 $\pm44.5\mu m$ , respectively.

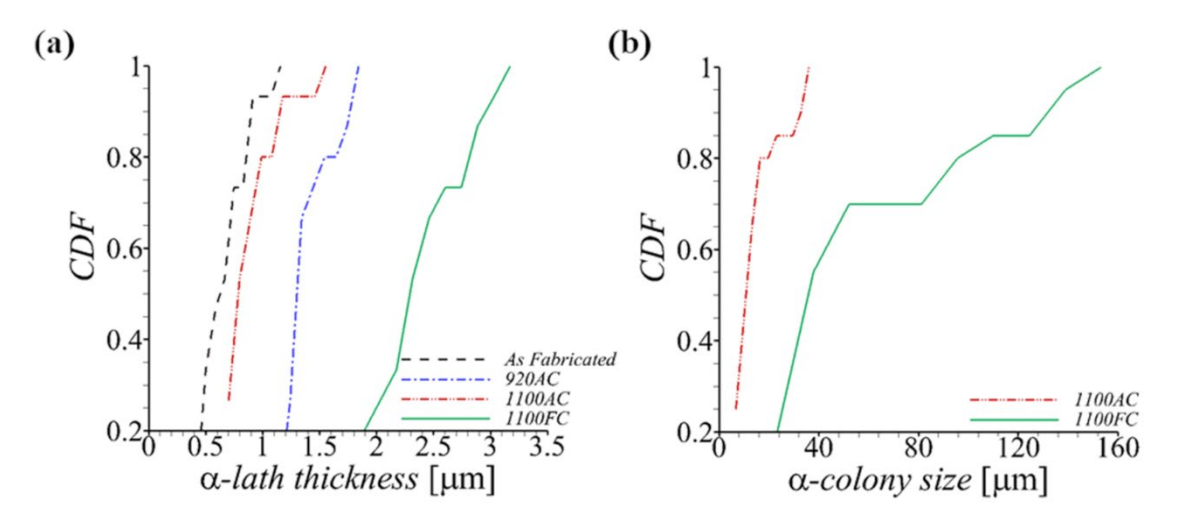


Figure 2: The cumulative distribution function (CDF) of the  $\alpha$ -phase (a) laths and (b) colonies in the microstructures of the as fabricated and all post-process heat-treated materials.

## 3.2 Mechanical response

The mechanical response characterized using unpolished and unetched SENT specimens of the as fabricated and three post-process heat-treated materials are shown in Fig. 3. The geometry and dimensions of the SENT specimens utilized in this work are shown in Fig. 3(a). The variation of the force normalized by the minimum cross-section area with the displacement normalized by the gauge length of the SENT specimens are shown in Fig. 3(b). As can be seen in the figure, for all materials, the normalized force initially increases almost linearly with the normalized displacement before reaching a maximum value. This maximum value is followed by a monotonic drop in the load carrying capacity. The maximum normalized force for the as fabricated, 920AC, 1100AC, and 1100FC materials is roughly  $850 \pm 50$ MPa,  $853 \pm 48$ MPa,  $842 \pm 60$ MPa, and  $817 \pm 30$ MPa, respectively. The maximum force in the normalized force-displacement curves correspond to the onset of slight through thickness necking near the notch tip. The cross on the normalized force-displacement curves in Fig. 3(b) (as well as in Figs. 3(c) and (d)) marks the observation of nucleation of a crack from the initial notch during the in-situ tests, which roughly coincides with the maximum force.

The variation of the normalized force with the notch tip opening and that of the notch tip opening with the normalized displacement are shown in Figs. 3(c) and (d), respectively. The notch tip opening defined in Fig. 3(a) provides an estimate of the local deformation at the notch tip. The notch tip opening displacement, *b*, is estimated from the individual frames of the videos captured during the uninterrupted in-situ tests of the unpolished and unetched specimens. As can be seen in Fig. 3(c), for all materials, the normalized force first increases linearly with the notch tip opening which is followed by a non-linear regime wherein the normalized force increases with notch tip opening with continuously decreasing slope and finally reaches a maximum value. Post maxima the normalized force decreases gradually with increasing notch tip opening. The post maxima gradual decrease in the normalized force with increasing notch tip opening is because post maxima (which coincides with the onset of through thickness necking) the deformation localizes near the notch tip. The deformation localization near the notch tip is evident from Fig. 3(d) where the notch tip opening can be seen to increase rapidly for the values of normalized displacement greater than the value corresponding to the maximum normalized force. The value of notch tip opening at crack

nucleation for as fabricated, 920AC, 1100AC and 1100FC materials is roughly  $0.62 \pm 0.35$ ,  $0.85 \pm 0.26$ ,  $0.65 \pm 0.31$ , and  $0.81 \pm 0.21$ , respectively.

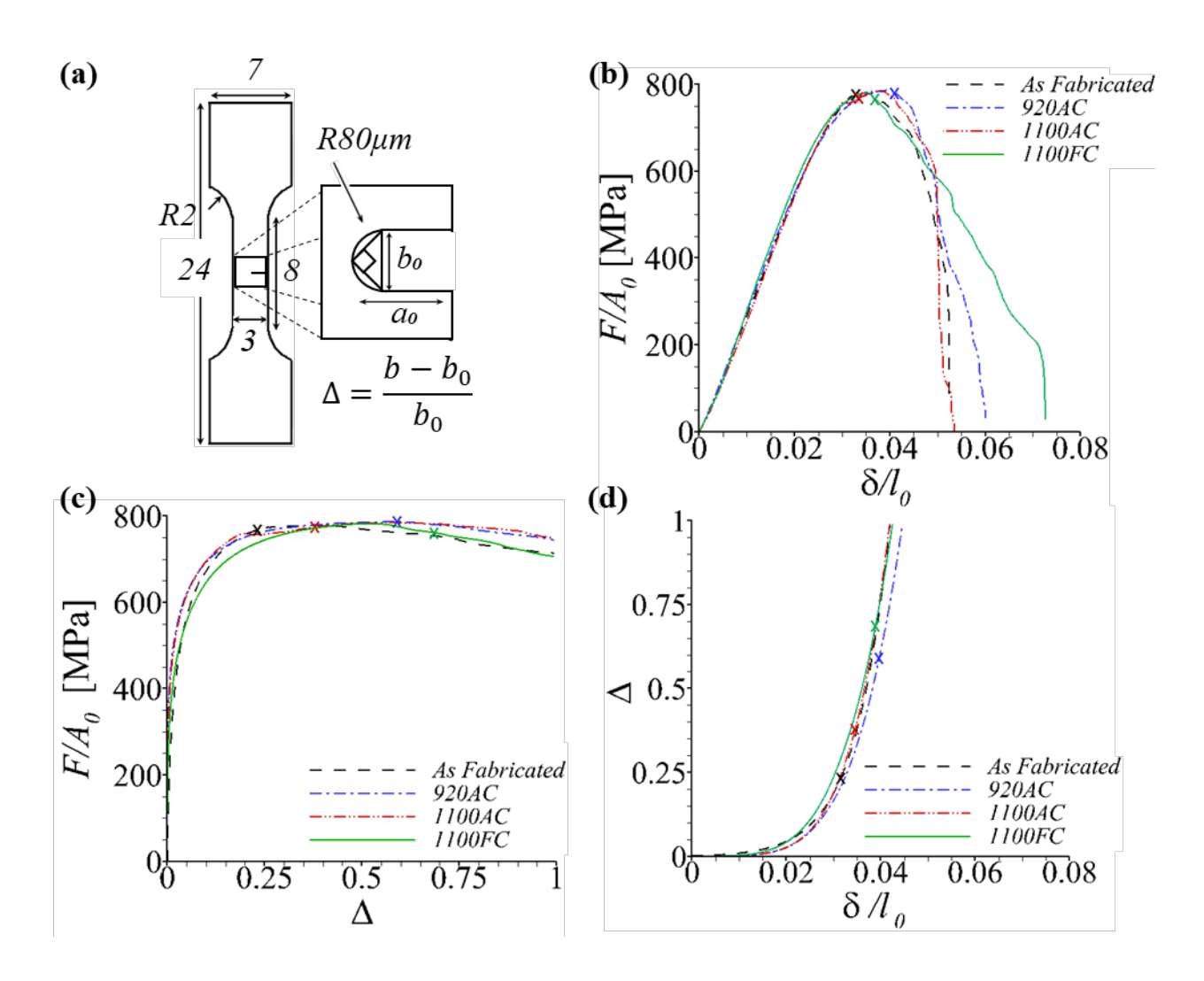


**Figure 3: (a)** A schematic showing the geometry and dimensions (in mm) of the single-edge notch tension (SENT) specimen and the definition of the notch tip opening,  $\Delta$ . (b) Selected but typical force, F, (normalized by minimum initial cross-section area,  $A_0$ ) versus displacement,  $\delta$ , (normalized by initial gauge length,  $l_0$ ) response, (c) normalized force versus notch tip opening response, and (d) Notch tip opening vs normalized displacement response of the SENT specimens of as fabricated and all post-process heat-treated materials. The symbol 'x' in (b)-(d) marks the point in the deformation history at which a crack is first observed during the in-situ experiments.

The values of the maximum normalized force in Fig. 3(b) and that of the notch tip opening at crack nucleation in Fig. 3(c) for the as fabricated and post-process heat-treated materials are shown in

Figs. 4(a) and (b), respectively. The ultimate tensile strength of all the four materials obtained in Draelos et al. (2020) using unpolished and unetched flat dog-bone specimens are also plotted in Fig. 4(a). The maximum normalized force sustained by the specimens provides a measure of the notch strength and a comparison of this quantity with the ultimate tensile strength provides an estimate of the extent of notch weakening in the material. The data in Fig. 4(a) shows that the as fabricated material undergoes significant notch weakening while the three post-process heat-treated materials does not undergo statistically significant notch weakening. The data in Fig. 4(b) shows that the values of notch tip opening at crack nucleation are statistically the same for the as fabricated and 1100AC specimens, while those of the 920AC and 1100FC specimens can be more than 30% greater than that of the as fabricated specimens. However, a significant decrease in the tensile elongation of the dog-bone specimens of EBM-processed Ti-6Al-4V was observed after super-transus heat treatment by Draelos et al. (2020). They reported an approximately 15% and 30% decrease in tensile elongation of 1100FC and 1100AC specimens, respectively, compared to the as-fabricated specimens.

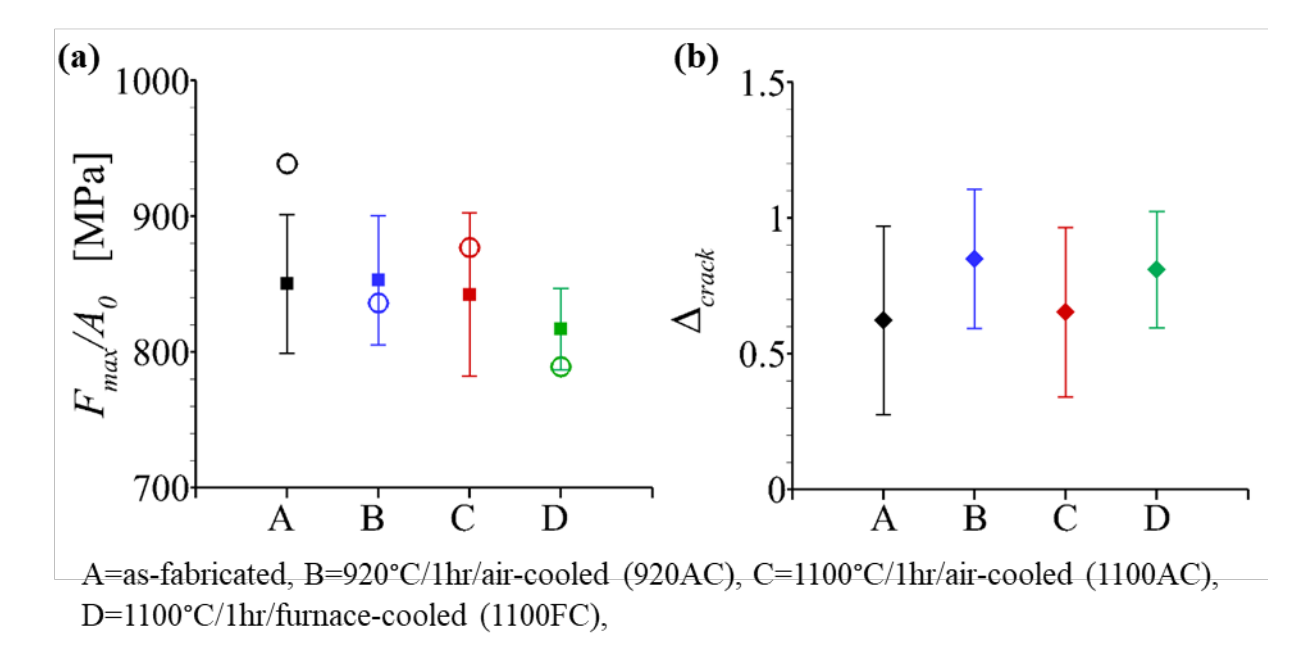


**Figure 4: (a)** The values of the maximum normalized force,  $F_{max}/A_0$ , sustained by the SENT (closed symbols) and dog-bone (open symbols, data is from Draelos et al. (2020)) specimens, and **(b)** the values of the notch tip opening at which a crack is first observed during the SENT in-situ experiments,  $\Delta_{crack}$ , for the as fabricated and post-process heat-treated materials.

# 3.3 Microstructural-scale deformation characteristics

In this section we present the evolution of the microstructure and microstructural-scale planar deformation field on the surface of the mechanically polished and slightly etched SENT specimens. Figure 5 shows the high-resolution optical micrographs of the microstructure on the surface of the as fabricated material at six values of the imposed normalized tensile displacement. The location of the notch in the specimen is marked in Fig. 5(a) and the axis of the columnar prior  $\beta$ -phase grains is parallel to the loading direction. The increase in the deformation close to the notch tip with increasing tensile displacement can be seen in Figs. 5(b)-(d). The deformation near the notch tip takes a shape like the forewings of a butterfly. However, with increasing tensile displacement one of the forewing shaped deformation zones grows more than the other one, thus, making it asymmetric. Nevertheless, two small cracks eventually emanate along the center line of both forewing shaped deformation zones from the deformed notch tip, Fig. 5(d). These cracks are inclined at roughly  $\pm 45^{\circ}$  with respect to the orientation of the initial notch. With further increase in the imposed tensile displacement, the crack along the fastest growing forewing shaped deformation zone becomes dominant and continues to grow while the other one is arrested. As the dominant crack grows though the ligament its inclination with respect to the initial notch continues to decrease i.e., it grows more and more straight ahead. The inclination of the dominant crack is roughly 30° and 15° with respect to the initial notch in Figs. 5(e) and (f), respectively.

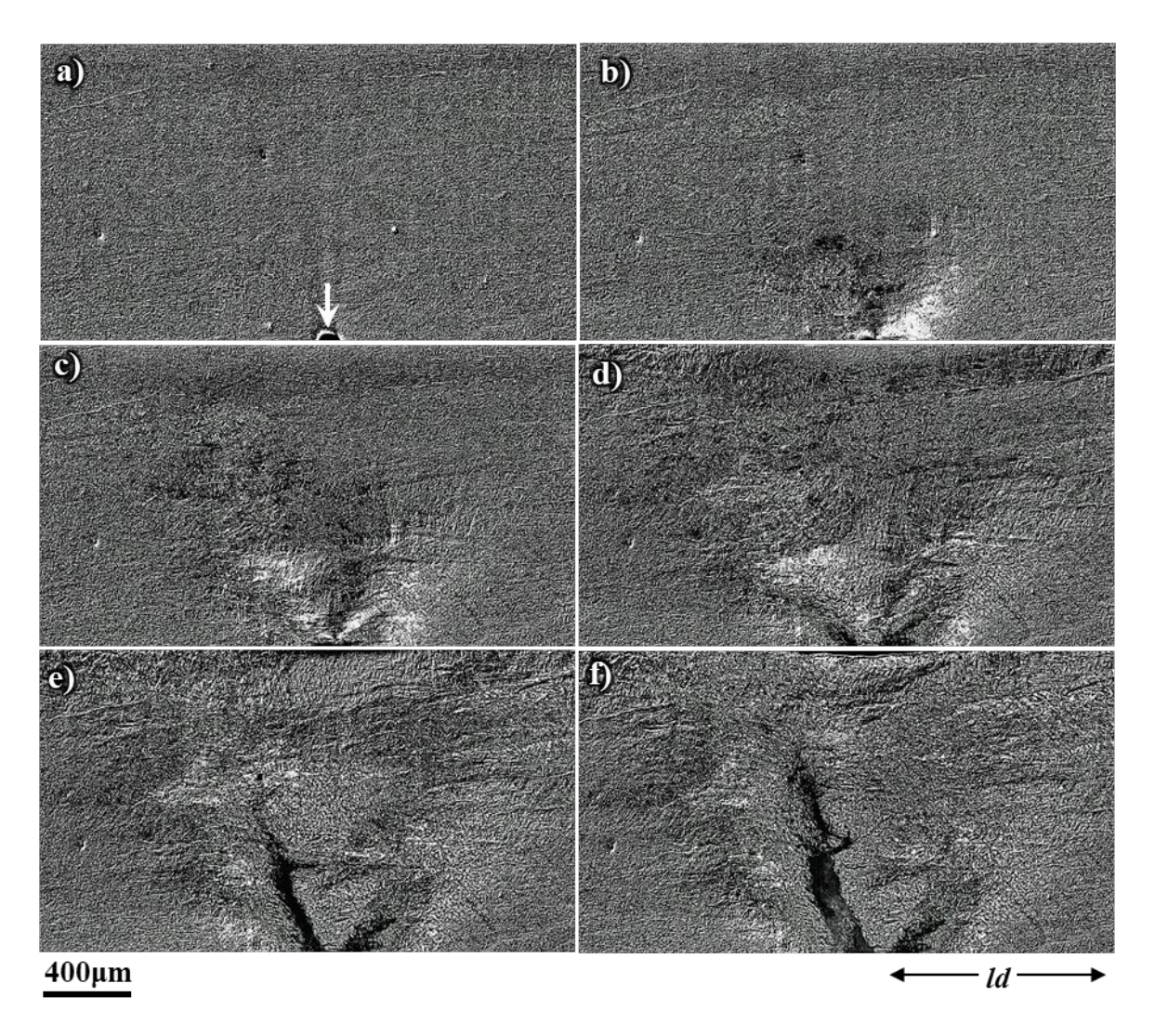
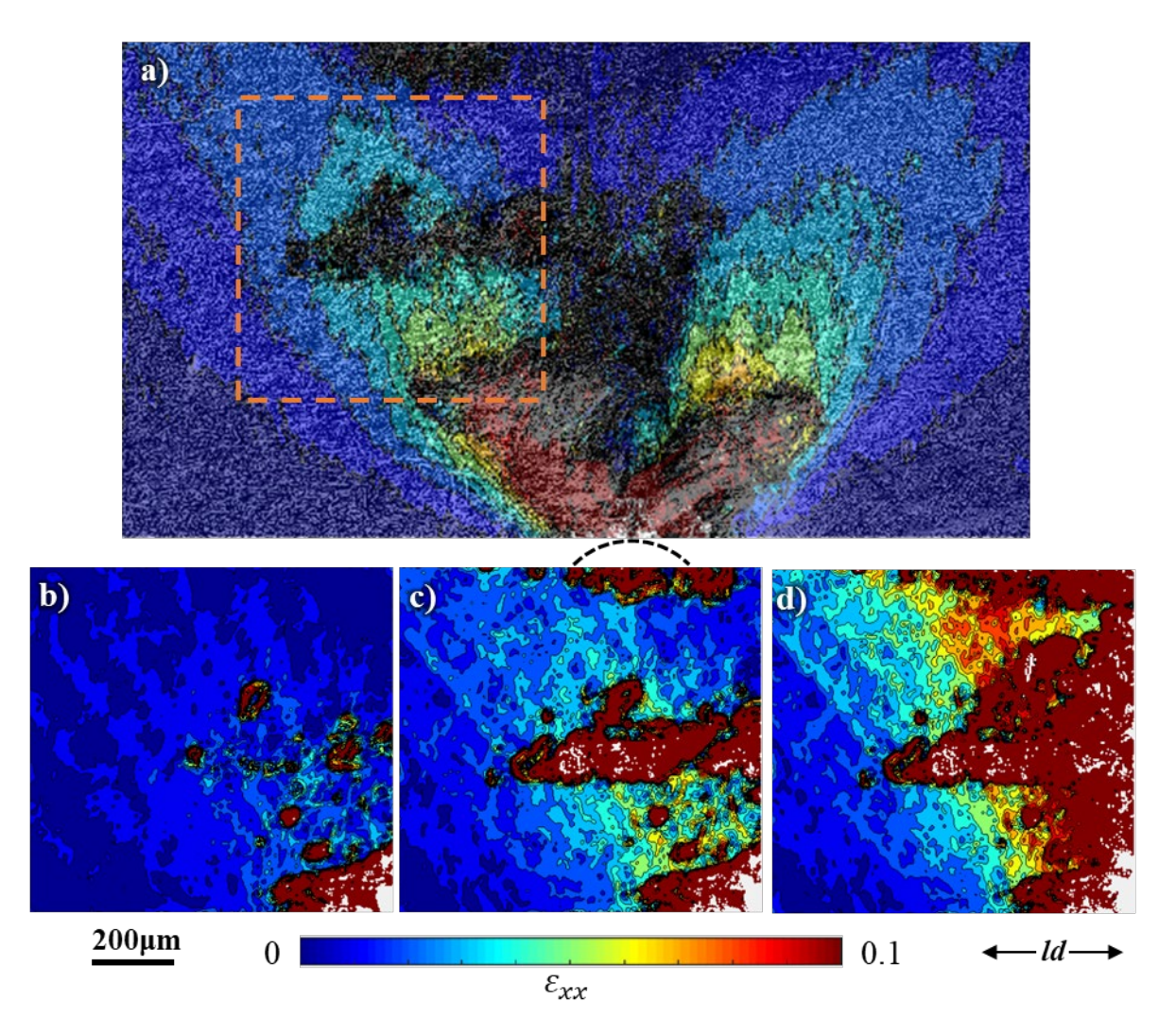


Figure 5: (a)-(f) Optical micrographs of the microstructure on the surface of a SENT specimen of the as fabricated material at imposed normalized displacements,  $\delta/l_0$ , of 0, 0.024, 0.03, 0.036, 0.043, and 0.046, respectively. The loading direction is ld, the arrow in (a) marks the initial notch tip location, and the scale bar is the same in (a)-(f).

The microstructure-scale distribution of the axial strain on the surface of the as fabricated material at an imposed normalized tensile displacement,  $\delta/l_0 = 0.03$  is shown in Fig. 6(a). The location of the notch in the specimen is also marked in Fig. 6(a) and the axis of the columnar prior  $\beta$ -phase grains is parallel to the loading direction. The distribution of the axial strain now clearly shows the asymmetric butterfly forewing shaped deformation pattern at the deformed notch tip. The distribution of the axial strain in a smaller region away from the notch tip is shown in Figs. 6(b)-(d) at three values of the imposed tensile displacement. The white spots in these figures represent the uncorrelated regions where the strain values are not estimated. As can be seen in these figures,

the deformation in the material is not uniform and is localized in bands that are oriented parallel to the loading direction. The width of these bands is roughly of the order of the width of the prior  $\beta$ -phase grains (see Fig. 1(a) for reference). This implies that the deformation away from the notch occurs more favorably in some prior  $\beta$ -phase columnar grains than others, but as the imposed tensile displacement increases more and more grains start to deform, see Figs. 6(b)-(d).



**Figure 6: (a)** The variation of the axial strain,  $\varepsilon_{\chi\chi}$ , (with x-axis being ld) ahead of the deformed notch on the surface of a SENT specimen of the as fabricated material at an imposed normalized displacement,  $\delta/l_0=0.03$ . The contour plot in (a) is superimposed on the top of the optical image of the deformed microstructure. **(b)-(d)** The variation of  $\varepsilon_{\chi\chi}$  in a smaller region outlined in (a) at  $\delta/l_0=0.024$ , 0.03 and 0.036. The loading direction is ld, the dotted curve under (a) indicates the notch location, and the scale bar is the same in (a)-(d).

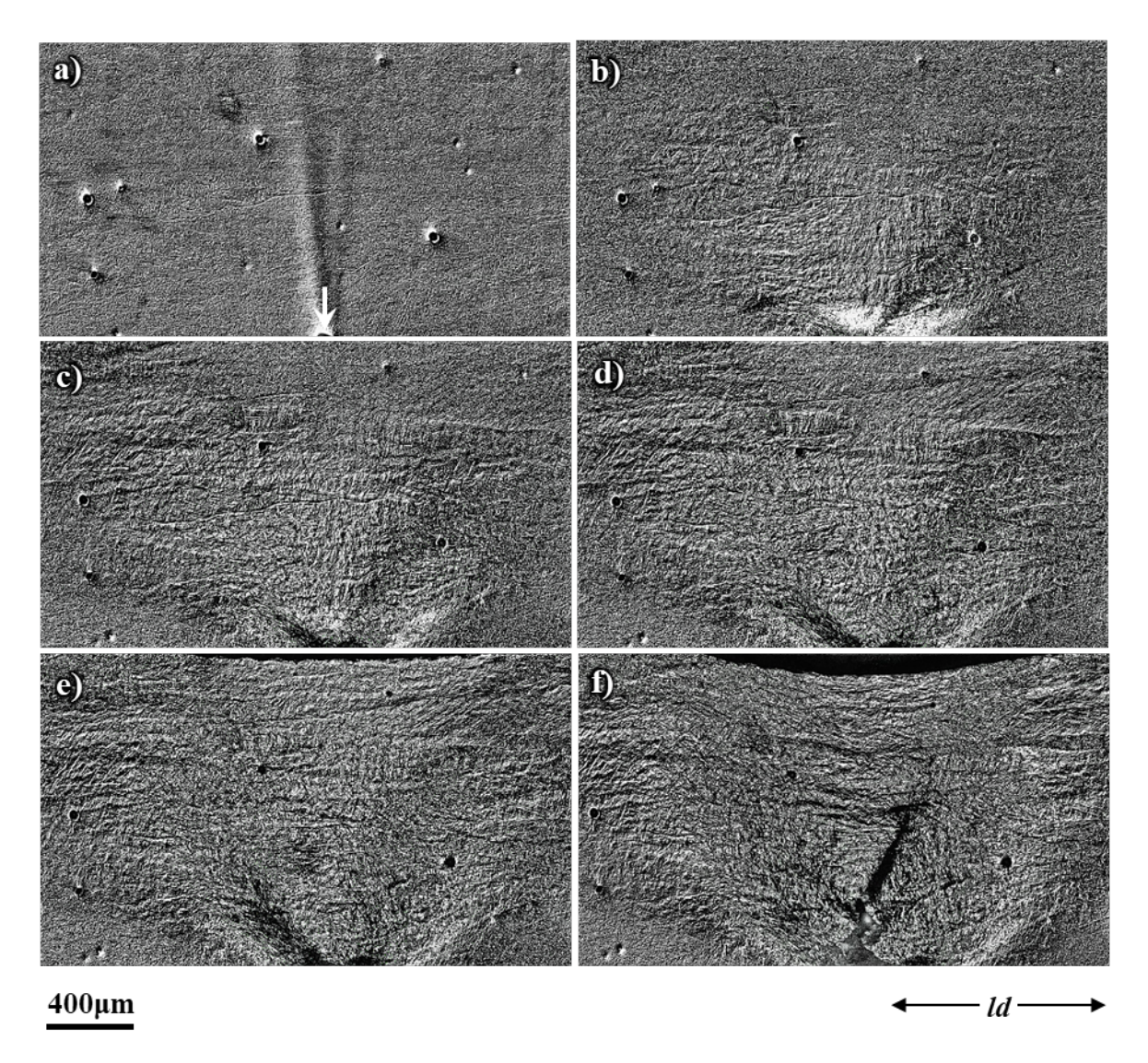
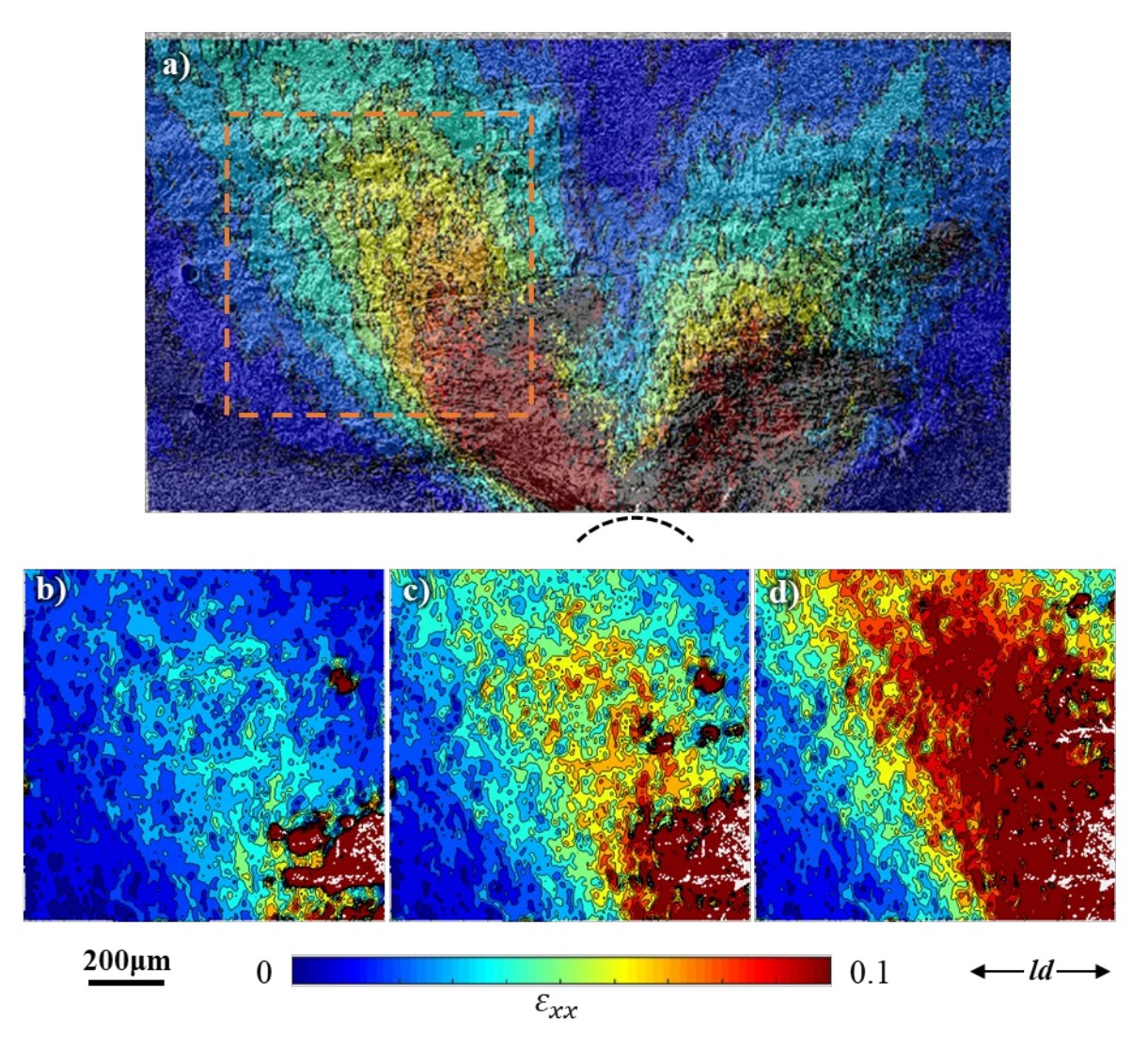


Figure 7: (a)-(f) Optical micrographs of the microstructure on the surface of a SENT specimen of 920°C/1hour/air-cooled (920AC) material at imposed normalized displacements,  $\delta/l_0$ , of 0, 0.024, 0.031, 0.037, 0.043, and 0.049, respectively. The loading direction is ld, the arrow in (a) marks the initial notch tip location, and the scale bar is the same in (a)-(f).

The high-resolution optical micrographs of the microstructure on the surface of a SENT specimen of the 920AC material at six values of the imposed normalized tensile displacement are shown in Fig. 7. The location of the notch in the specimen is marked in Fig. 7(a) and the axis of the initial columnar prior  $\beta$ -phase grains is parallel to the loading direction. As in Fig. 5, the increase in the deformation close to the notch tip with increasing tensile displacement can be seen in Fig. 7. Also, here as well, the deformation near the notch tip takes a shape like the forewings of a butterfly but is not as obvious from the optical micrographs in Fig. 7 as is the case in Fig. 5. However, in the

SENT specimens of the 920AC material crack from the notch tip nucleates at slightly greater values of the imposed normalized displacement, see Fig. 3(b), and notch tip opening, see Fig. 4(b), compared to that of the as fabricated material. The crack nucleation is preceded by relatively greater through thickness necking and only one dominant crack nucleates from the notch tip in the SENT specimens of the 920AC material. Post nucleation, the crack does follow a slightly zig-zag path in the beginning, but mostly grows straight ahead.



**Figure 8:** (a) The variation of the axial strain,  $\varepsilon_{\chi\chi}$ , (with x-axis being ld) ahead of the deformed notch on the surface of a SENT specimen of 920°C/1hour/air-cooled (920AC) material at an imposed normalized displacement,  $\delta/l_0=0.043$ . The contour plot in (a) is superimposed on the top of the optical image of the deformed microstructure. (b)-(d) The variation of  $\varepsilon_{\chi\chi}$  in a smaller region outlined in (a) at  $\delta/l_0=0.036$ , 0.043 and 0.049. The loading direction is ld, the dotted curve under (a) indicates the notch location, and the scale bar is the same in (a)-(d).

The distribution of the microstructure-scale axial strain in Fig. 8(a) on the surface of the 920AC material at an imposed  $\delta/l_0 = 0.043$  now clearly shows the butterfly forewing shaped deformation pattern emanating from the deformed notch tip. As in Fig. 6(a), here as well, the butterfly forewing shaped deformation pattern is asymmetric. However, the distribution of the axial strain within the asymmetric butterfly forewing shaped deformation zones are relatively more uniform compared to that in the SENT specimens of the as fabricated material. This can be seen more clearly in the higher magnification view of the strain distribution in a smaller region away from the notch tip that are shown in Figs. 8(b)-(d) at three values of the imposed tensile displacement.

Figure 9 shows the high-resolution optical micrographs of the microstructure on the surface of the 1100AC material at six values of the imposed normalized tensile displacement. The location of the notch in the specimen is marked in Fig. 9(a) and the loading direction is marked as ld. Also, the microstructure-scale distribution of the axial strain on the surface of this specimen at an imposed normalized tensile displacement,  $\delta/l_0 = 0.03$  is shown in Fig. 10(a). As can be seen in Fig. 9 and Fig. 10(a), the size of the deformation zone near the notch tip is much greater in the SENT specimens of the 1100AC material compared to those of the as fabricated and 920AC materials at any comparable imposed tensile displacement. Furthermore, the shape of the deformation zone is no more like the forewings of a butterfly as is the case for the as fabricated and 920AC materials, but instead they are like thick bands inclined at roughly  $\pm 30^{\circ}$  with respect to the orientation of the initial notch in Fig. 10(a).

The SENT specimens of the 1100AC material undergo significantly less through thickness necking at the notch tip compared to that of the 920AC material. Like the as fabricated material here as well two cracks initially nucleate from the deformed notch tip, Fig. 9(e), and only one of the cracks continues to grow. However, unlike the as fabricated and 920AC materials, in 1100AC material, microcracks ahead of the growing crack appear on the surface of the specimen. Almost all these microcracks form in the  $\alpha$ -phase along the prior  $\beta$ -phase grain boundaries. One such grain boundary is marked with a dashed-line in Fig. 9(a) and its continued deformation leading to the formation of a microcrack on the specimen surface is tracked using an arrow in Figs. 9(b)-(f). As

can be qualitatively seen in these figures, the marked grain boundary undergoes large deformation and eventually starts to open like a microcrack, Fig. 9(f).

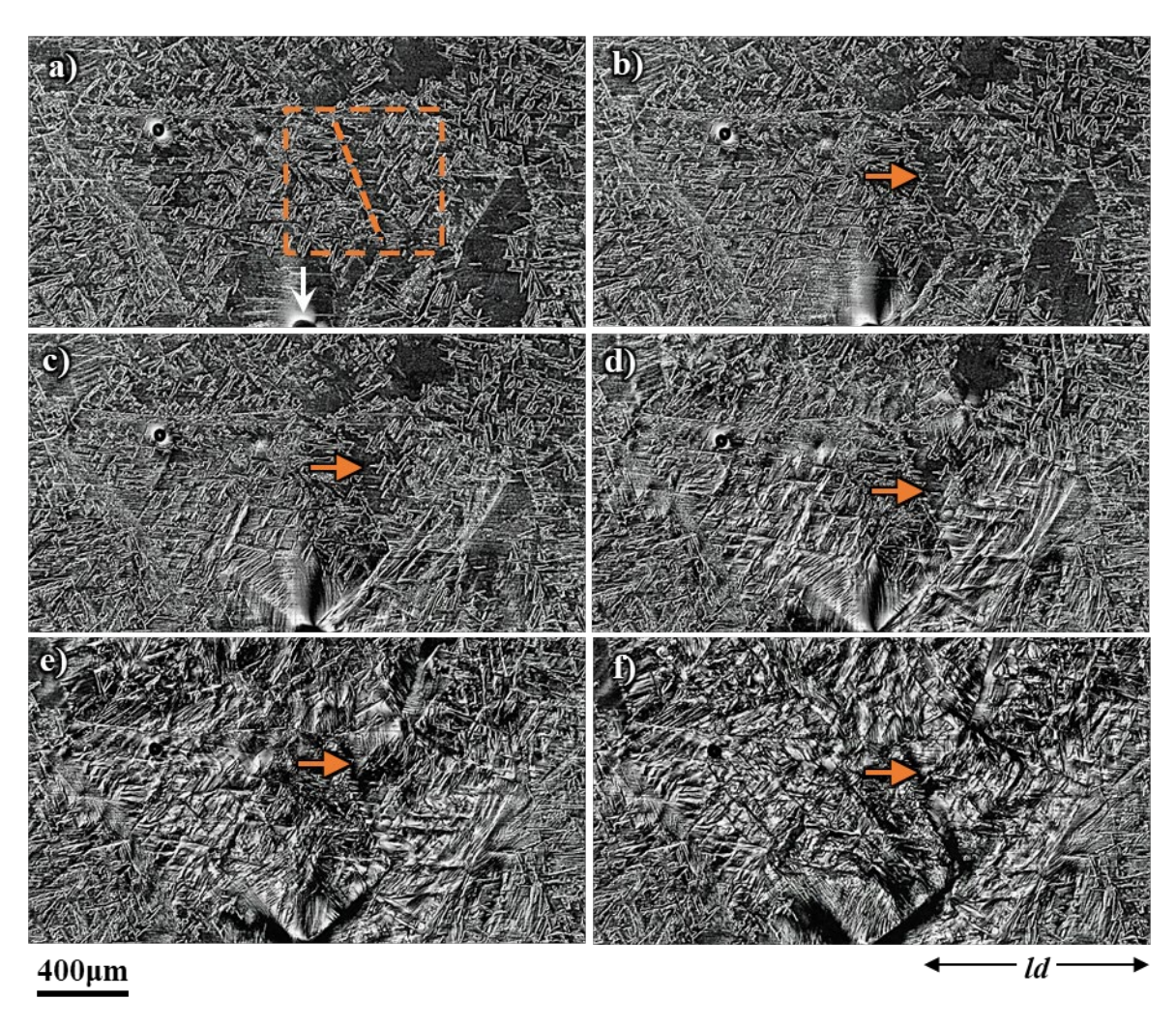
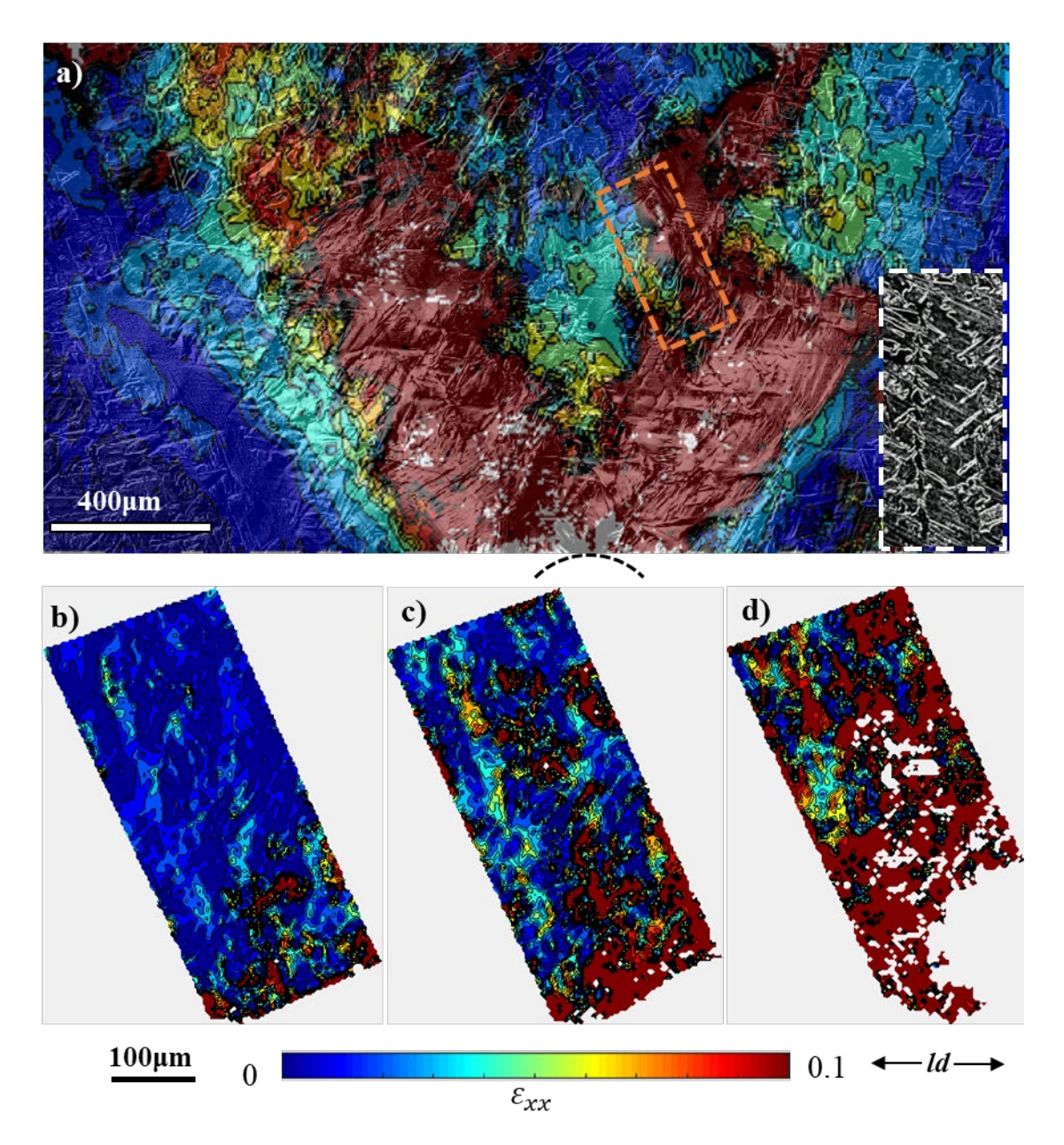


Figure 9: (a)-(f) Optical micrographs of the microstructure on the surface of a SENT specimen of  $1100^{\circ}$ C/1hour/air-cooled (1100AC) material at imposed normalized displacements,  $\delta/l_0$ , of 0, 0.018, 0.025, 0.03, 0.037, and 0.044, respectively. The loading direction is ld, the arrow in (a) marks the initial notch tip location, and the scale bar is the same in (a)-(f).

The distribution of axial strain in a small region encompassing a prior  $\beta$ -phase grain boundary away from the notch (as outlined in Fig. 10(a)) at three values of the imposed tensile displacement are shown in Figs. 10(b)-(d). The initial microstructure of this small region is shown as an inset in Fig. 10(a). The white spots in Figs. 10(b)-(d) represent the uncorrelated regions where the strain values cannot be estimated due to extremely large local deformation. As can be seen in these figures, with increasing imposed tensile displacement, discrete regions of extremely high strain

values form along the boundary. The discreteness in the strain hot-spots is likely due to the non-uniformity in the thickness of the grain boundary  $\alpha$ -phase layer, see the insert in Fig. 10(a). The average value of the axial strain in the strain hot-spots along the grain boundary in Fig. 10(c) is roughly 0.4 which is almost 12-times greater than the strain values surrounding the grain boundary region.

The high-resolution optical micrographs of the microstructure on the surface of a SENT specimen of the 1100FC material at six values of the imposed normalized tensile displacement are shown in Fig. 11. The location of the notch in the specimen is marked in Fig. 11(a) and the loading direction is marked as ld. As can be seen in these figures, the size of the deformation zone near the notch tip is somewhat comparable to the 1100AC material at comparable imposed tensile displacements. However, the deformation ahead of the notch tip is much more discrete and appears to be concentrated in select colonies of  $\alpha$ -phase lamellae within a prior  $\beta$ -phase grain. So that some colonies of  $\alpha$ -phase lamellae undergo significantly more deformation compared to others. The large deformation contrast between two colonies gives rise to nucleation of a microcrack along the colony-colony boundary. The nucleation of a microcrack along the colony-colony boundary occurs at multiple locations ahead of the deforming notch tip even before a crack nucleates from the deformed tip. The final fracture of the specimen occurs after a crack nucleates from the deformed notch tip and links up with the microcracks along the colony-colony boundaries that are in proximity.



**Figure 10: (a)** The variation of the axial strain,  $\varepsilon_{xx}$ , (with x-axis being ld) ahead of the deformed notch on the surface of a SENT specimen of  $1100^{\circ}\text{C/1hour/air-cooled}$  (1100AC) material at an imposed normalized displacement,  $\delta/l_0=0.03$ . The contour plot in (a) is superimposed on the top of the optical image of the deformed microstructure. **(b)-(d)** The variation of  $\varepsilon_{xx}$  in a smaller region outlined in (a) at  $\delta/l_0=0.025$ , 0.03 and 0.037. The loading direction is ld, the dotted curve under (a) indicates the notch location, and the scale bar is the same in (a)-(d). The insert in (a) shows the initial microstructure of the region highlighted by a dashed-box in the contour plot.

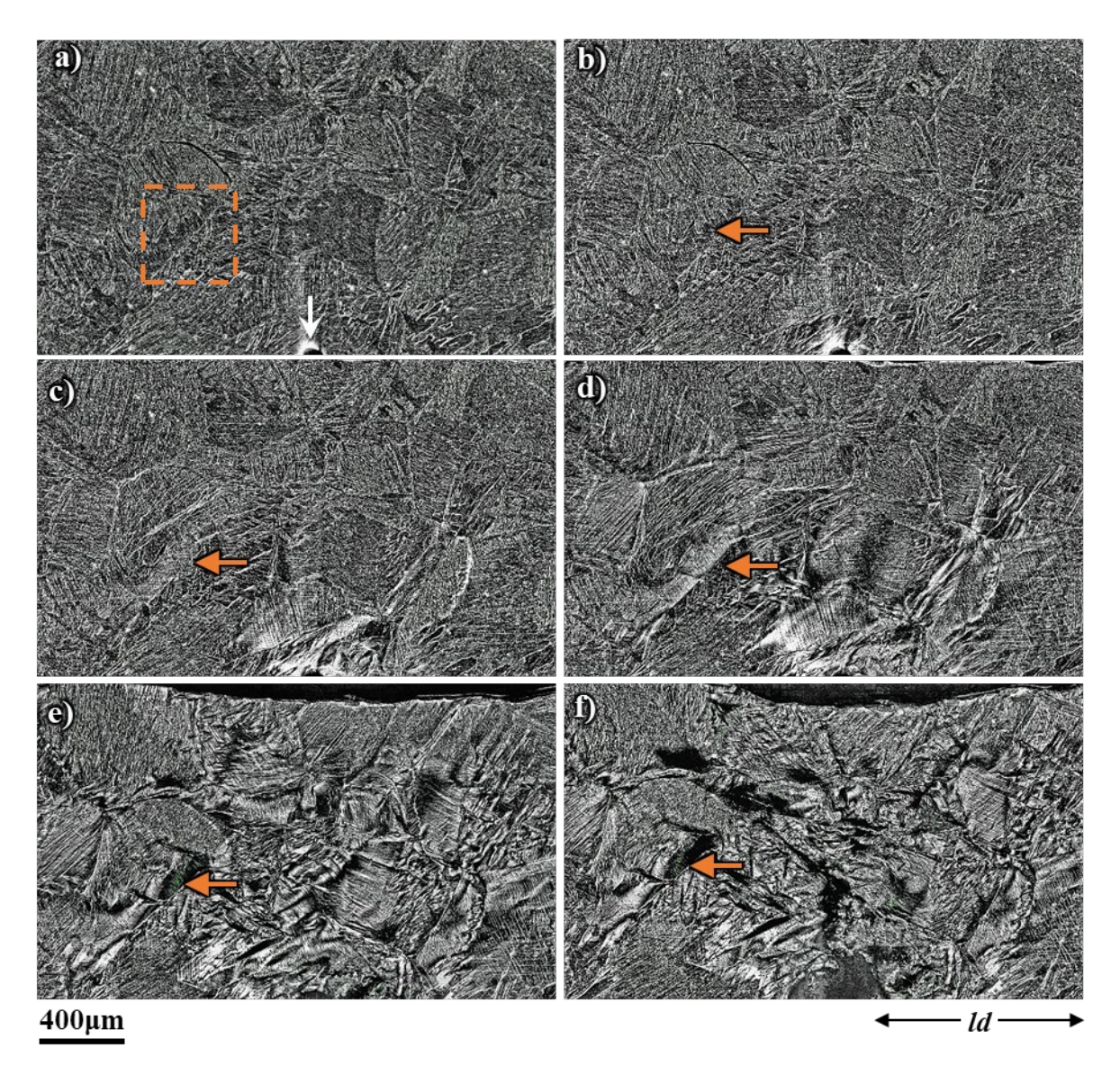


**Figure 11:** (a)-(f) Optical micrographs of the microstructure on the surface of a SENT specimen of  $1100^{\circ}$ C/1hour/furnace-cooled (1100FC) material at imposed normalized displacements,  $\delta/l_0$ , of 0, 0.028, 0.035, 0.042, 0.06, and 0.066, respectively. The loading direction is ld, the arrow in (a) marks the initial notch tip location, and the scale bar is the same in (a)-(f).

One colony-colony boundary is marked with a dashed-box in Fig. 11(a) and its continued deformation leading to the formation of a microcrack on the specimen surface is tracked using an arrow in Figs. 11(b)-(f). Also, the zoomed in view of this same region at the same imposed tensile deformation levels are shown in Figs. 12(a)-(f). As can be seen in the sequence of images in Fig. 12, the colony above the colony-colony boundary highlighted with a dashed-line, Fig. 12(a), starts

to deform early on and continues to undergo significantly large deformation compared to the colony below the boundary. The deformation in the colony above the colony-colony boundary continues to increase with the increase in the imposed (far-field) tensile deformation. It should be noted that as the deformation concentrates in the colony above the boundary, the colony below the boundary will start to undergo (at least) partial unloading since the material at the macroscopic level does not exhibit significant strain hardening. Next, with continued deformation, the material in the colony above the colony-colony boundary starts to separate away from the boundary, Figs. 12(d)-(e). Finally, a semielliptical shaped microcrack of hundreds of microns in length nucleates in the preferentially deforming colony and at the colony-colony boundary, Fig. 12(f).

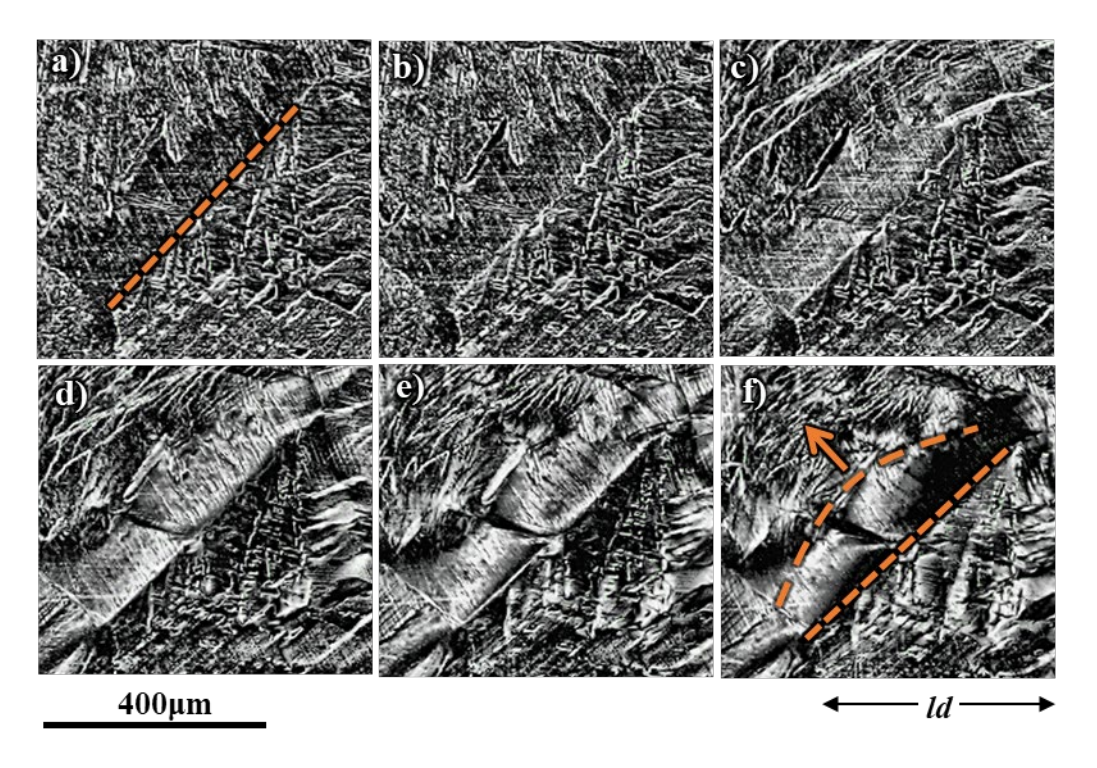


**Figure 12:** (a)-(f) Zoomed in optical micrographs of the region marked with a dashed-box in Fig. 11(a) for a SENT specimen of  $1100^{\circ}$ C/1hour/furnace-cooled (1100FC) material. The loading direction is ld, the dashed-line in (a) marks the boundary between two colonies of  $\alpha$ -phase lamellae, and the scale bar is the same in (a)-(f).

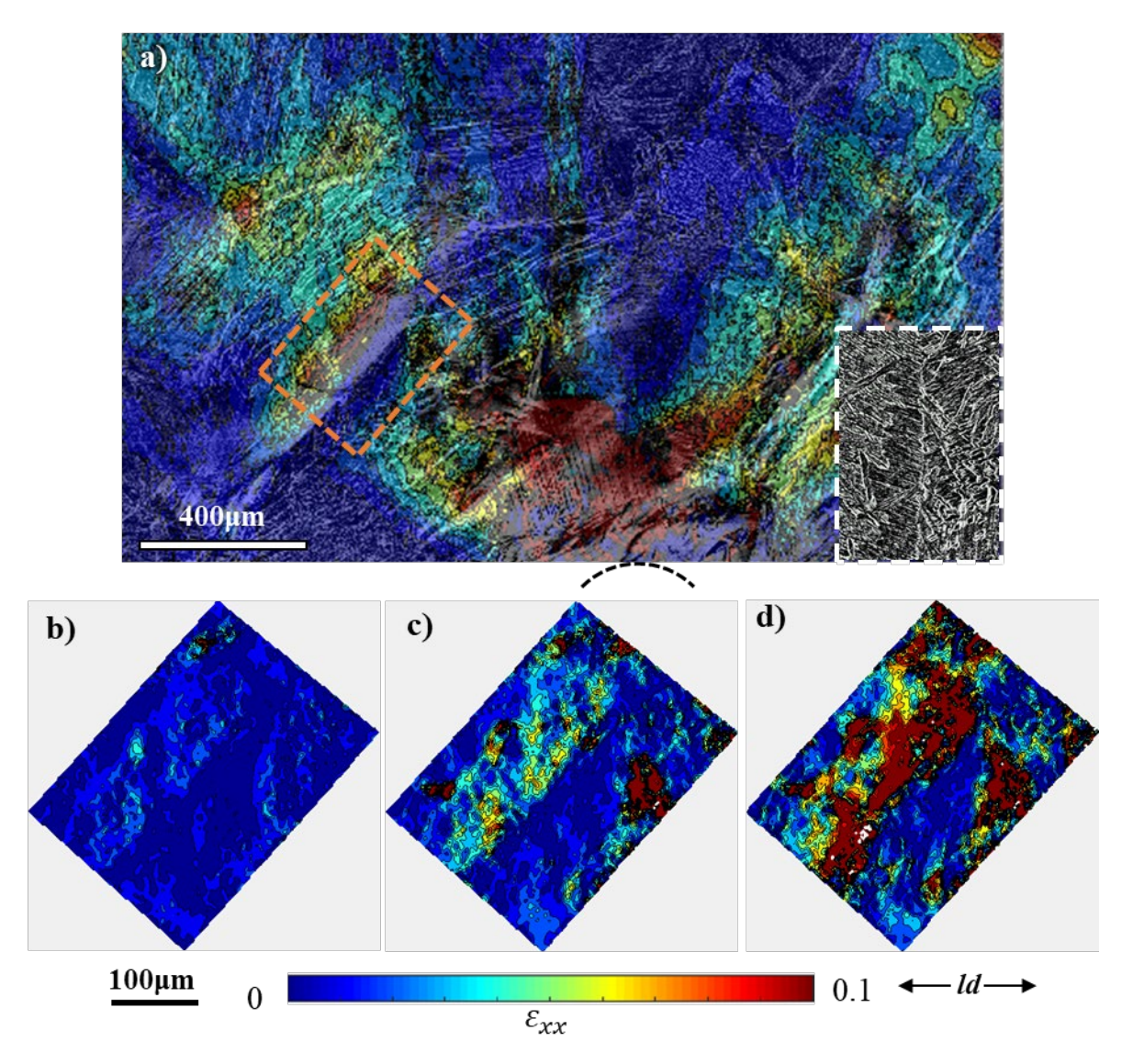


**Figure 13: (a)** The variation of the axial strain,  $\varepsilon_{\chi\chi}$ , (with x-axis being ld) ahead of the deformed notch on the surface of a SENT specimen of  $1100^{\circ}$ C/1hour/furnace-cooled (1100FC) material at an imposed normalized displacement,  $\delta/l_0=0.042$ . The contour plot in (a) is superimposed on the top of the optical image of the deformed microstructure. **(b)-(d)** The variation of  $\varepsilon_{\chi\chi}$  in a smaller region outlined in (a) at  $\delta/l_0=0.028$ , 0.035 and 0.042. The loading direction is ld, the dotted curve under (a) indicates the notch location, and the scale bar is the same in (a)-(d). The insert in (a) shows the initial microstructure of the region highlighted by a dashed-box in the contour plot.

The microstructure-scale distribution of the axial strain on the surface of the 1100FC material at an imposed  $\delta/l_0 = 0.042$  is shown in Fig. 13(a). The discreteness of the deformation ahead of the notch tip shown qualitatively in Fig. 11 can now be clearly seen in Fig. 13(a). The contrast between the deformation in two colonies across the same colony-colony boundary can also be seen in the region highlighted by a dashed-box in 12(a). The initial microstructure of the region highlighted by the dashed-box is also shown as an insert. Next, the distribution of the axial strain in the region highlighted by the dashed-box that encompasses a colony-colony boundary away from the notch at three values of the imposed tensile displacement are shown in Figs. 13(b)-(d). Note that the discreteness in the strain hot-spots in the colony above the colony-colony boundary is likely due to the non-uniformity of the microstructure, see the insert in Fig. 13(a). Nevertheless, the average value of the axial strain in the colony above the boundary is roughly 0.28 while in the colony just below the boundary is roughly 0.012. This is more than 20-times difference in the deformation level between the two colonies.

### 3.4 Fracture characteristics

Representative SE-SEM images of the fracture surfaces of the fractured SENT specimens of as fabricated and three post-process heat-treated materials are shown in Fig. 14. In Figs. 14(a)-(d) the initial notch is on the right side of the image and the crack propagated to the left as marked. The fracture surface of the as fabricated and 920AC material are roughly the same. Both materials underwent ductile fracture due to micro-void nucleation, growth, and coalescence as evident from the dimple morphology of the fracture surfaces, Figs. 14(a) and (b). The fracture surfaces of both of these materials also contain occasional regular and irregular large holes, see Figs. 14(a1)-(a2) and (b1)-(b2). These are likely pre-existing pores in the EBM processed material and are either surrounded by numerous fine micro-voids or quasi-cleavage region with signature of plastic deformation. The fracture surfaces of the 1100AC and 1100FC materials are significantly different from those of the as fabricated and 920AC materials. The fracture surfaces of these two materials contain multiple regions that comprise elongated grooves, like flutes. These flutes like regions are separated by regions with fine dimples. The remnant markings of the plastic deformation and occasional micro-voids are also clearly visible within the flutes, see Figs. 14(c1)-(c2) and (d1)-

(d2). A visible comparison of Fig. 14(c2) and (d1) clearly shows that width of the flutes in 1100AC material is much finer compared to those in the 1100FC material.

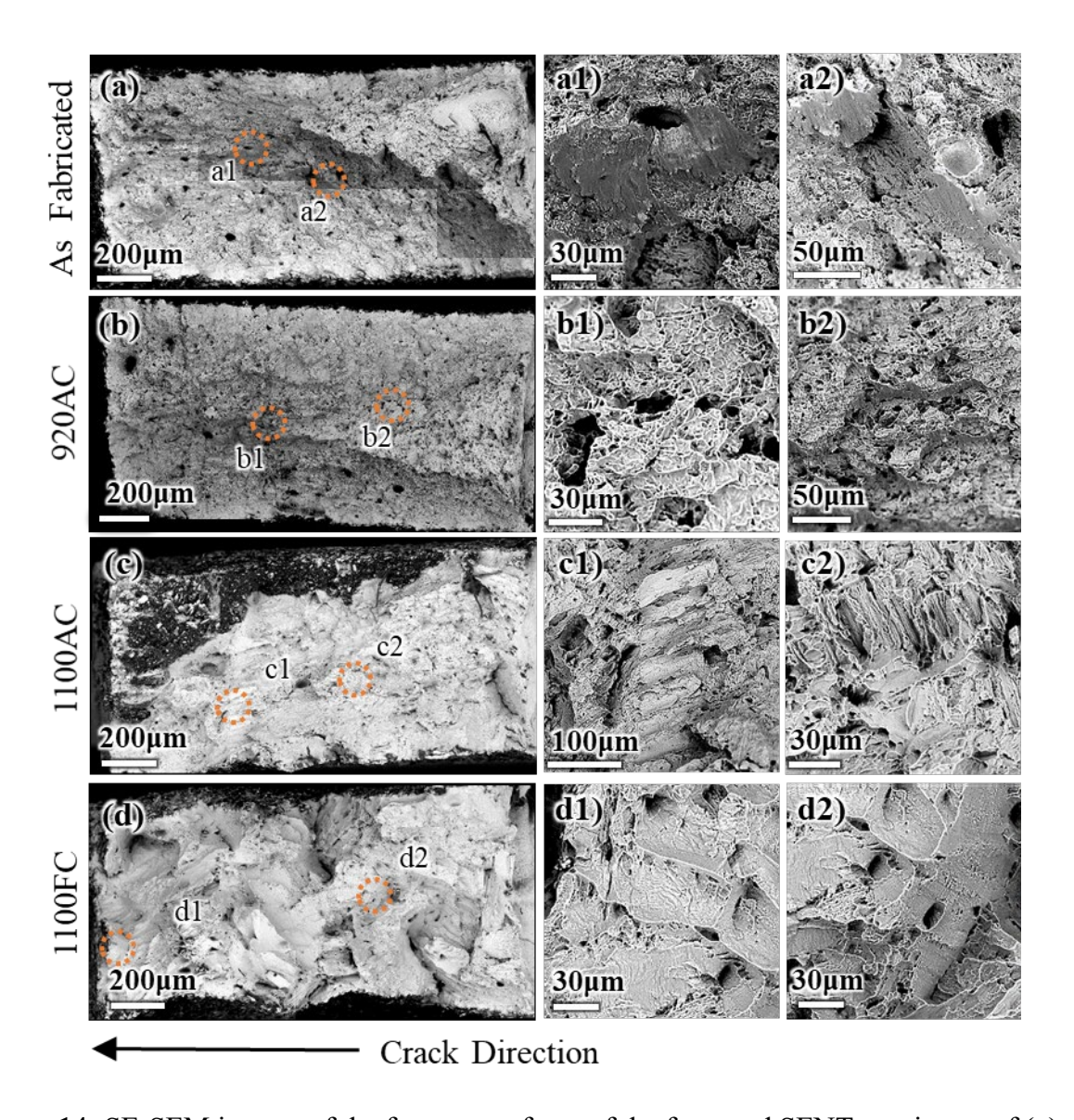


**Figure 14:** SE-SEM images of the fracture surfaces of the fractured SENT specimens of **(a)** as fabricated, **(b)** 920°C/1hr/air-cooled (920AC), **(c)** 1100°C/1hr/air-cooled (1100AC) and **(d)** 1100°C/1hr/furnace-cooled (1100FC) materials. Notch location is on the right in (a)-(d).

Figure 15 shows the SE-SEM images of the reconstructed fractured SENT specimens of 1100AC and 1100FC materials; and zoomed in views of the damage on the surface of the specimen away from the fracture surfaces in both the materials. The initial notch is located on the right side of Figs. 15(a) and (d), and the loading direction is marked as *ld*. In 1100AC material, a few long and

deep zig-zag surface cracks are observed away from the fracture surface as can be seen in Fig. 15(b). The half wavelength of these zig-zag cracks is roughly of the same order as that of the size of the prior  $\beta$ -phase grains. These (most likely) grain boundary cracks also contain semielliptical holes at the cusp of the zig-zag, Fig. 15(c). On the contrary, multiple small surface microcracks are observed in the 1100FC material, Fig. 15(e), and these microcracks are roughly semielliptical in shape, Fig. 15(f). Although not shown here, the reconstructed fractured SENT specimens of as fabricated and 920AC materials show column-like patterns along the axis of the specimens corresponding to the stretching of columnar prior  $\beta$ -phase grains. Also, none of the samples of these two materials show signs of any significant damage away from the fracture surface.

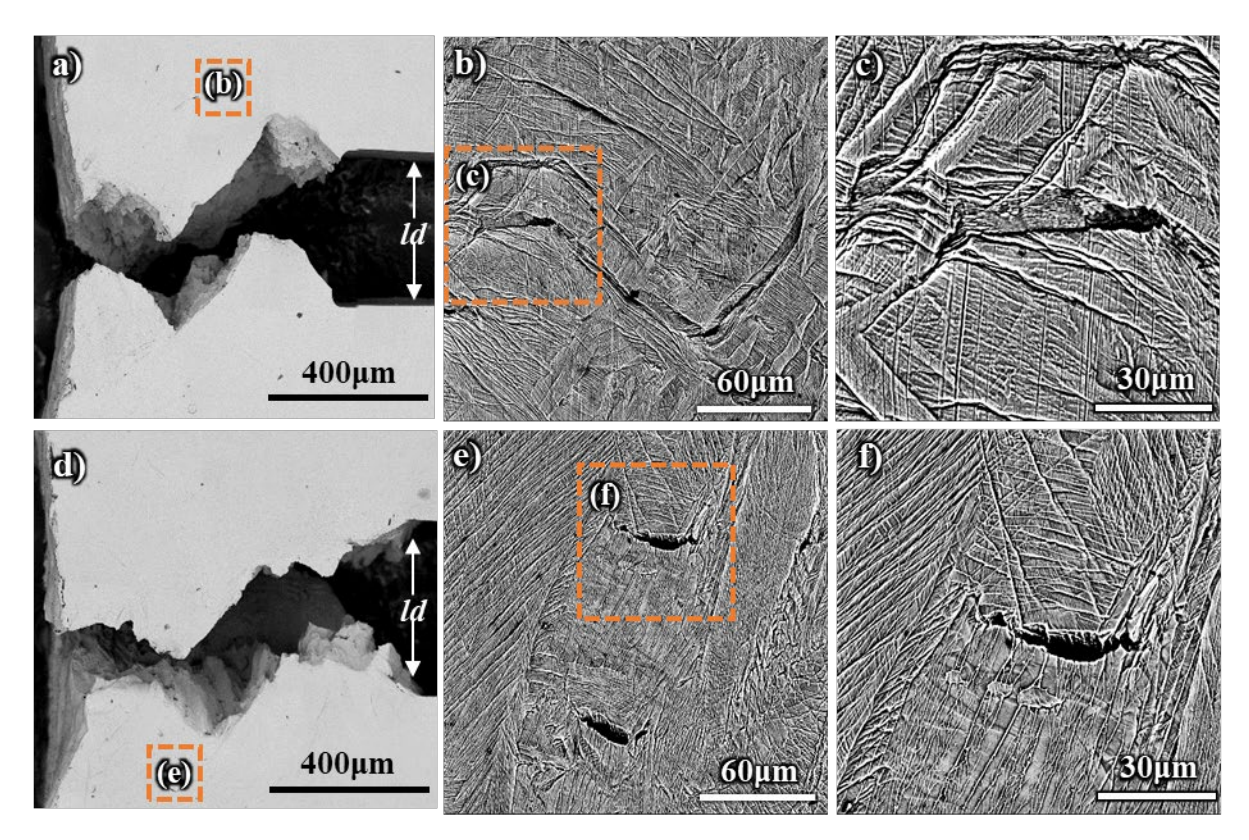


**Figure 15:** SE-SEM images of the surfaces of the fractured SENT specimens of (a)-(c) 1100°C/1hr/air-cooled (1100AC) and (d)-(f) 1100°C/1hr/furnace-cooled (1100FC) materials.

## 4. Discussion

The objective of this work is to better understand the microscale drivers and mechanisms of fracture in EBM processed Ti-6Al-4V subjected to various post-process heat-treatments. To this

end, the as fabricated material was subjected to one sub-transus heat-treatment followed by air-cooling and two super-transus heat-treatments followed by either air- or furnace-cooling. These resulted in two microstructure-types, one with columnar prior  $\beta$ -phase grains comprising basketweave  $\alpha$ -phase and intergranular  $\alpha$ -phase for the as-fabricated and sub-transus heat-treated materials, and second with equiaxed prior  $\beta$ -phase grains comprising colonies of  $\alpha$ -phase lamellae and intergranular  $\alpha$ -phase for the two super-transus heat-treated material. Next, a series of in-situ SENT tests was carried out under a high-resolution digital optical microscope. The panoramic high-resolution images captured during the in-situ tests were also used to characterize the planar deformation utilizing two-dimensional microstructure-based DIC to the extent possible. The results of the in-situ SENT tests together with microstructure-based DIC and post-mortem fractographic analyses now provide us with a clear understanding of the microstructure-fracture correlation of the as fabricated and all post-process heat-treated materials.

Our results show that the fracture mechanism of the as fabricated and sub-transus heat-treated materials with the same microstructure-type is essentially the same. Both materials fracture by a single dominant crack that grows following the well-known ductile fracture mechanism involving micro-void nucleation, growth, and coalescence. The only difference between the two materials is that the deformation pattern near the notch is relatively more uniform in the sub-transus heat-treated material than the as fabricated material. This is due to the slight coarsening of the microstructure and relaxation of the residual stresses resulting from the sub-transus heat-treatment. These findings are in line with the prior observations that the sub-transus heat-treatment of the as fabricated material results in a decrease in both the yield and tensile strengths without significantly affecting the ductility of the material (de Formanoir et al., 2016, Draelos et al., 2020, Nandwana et al., 2019).

The change in the microstructure-type following the super-transus heat-treatments of the as fabricated material significantly changes the fracture mechanism. In this case, several microcracks of hundreds of microns in length first nucleate away from the deformed notch following extreme deformation at discrete locations. These microcracks then link up with the main crack that nucleates from the deformed notch leading to the final fracture of the specimen. The nucleation of a microcrack as a result of extremely localized deformation has also been observed in an aluminum

(Al 6061) alloy by Gross and Ravi-Chandar (2017). In Al 6061, microcracks of tens of microns in length were shown to nucleate as a result of extreme deformation within a shear band under the conditions of plane strain tension by using in-situ SEM imaging (Gross and Ravi-Chandar, 2017). Here we observed that in the super-transus heat-treated materials although the mechanism of microcrack nucleation is always roughly the same (i.e., due to extreme deformation), their location is extremely sensitive to the underlying microstructure.

In the super-transus air-cooled material, microcracks nucleate along the prior  $\beta$ -phase grain boundaries. The microcracks in this case form by the coalescence of multiple elongated grooves within a grain boundary facet that nucleate due to the extremely large (but not entirely uniform) plastic deformation of the grain boundary  $\alpha$ -phase. These appear as flutes on the fracture surfaces which confirms that they are not elongated dimples but are a result of the plastic deformation process. The localization of deformation in the grain boundary  $\alpha$ -phase occurs because the fine microstructural features (such as, size of the colonies of the  $\alpha$ -phase lamellae and the thickness of the  $\alpha$ -phase laths) in the air-cooled material limit the extent of plastic deformation within the prior  $\beta$ -phase grains as was shown in Draelos et al. (2020). The coarsening of the microstructural features in the furnace-cooled material allows for greater plastic deformation within prior  $\beta$ -phase grains as was also shown in Draelos et al. (2020). However, in this case plastic deformation within prior  $\beta$ -phase grains, occurs preferentially in select colonies of  $\alpha$ -phase lamellae. The preferential localization of deformation in one of the colonies across a colony-colony boundary results in the nucleation of a semielliptical groove like crack at the boundary. In both the super-transus heattreated materials, the crack growth also involves micro-void nucleation, growth, and coalescence, but this mechanism appears to be secondary and only assists in linking of microcracks with the main crack.

The in-situ small-scale SENT tests carried out in this work provided great insight into the micromechanisms of fracture in the EBM processed and post-process heat-treated Ti-6Al-4V, but these tests are not suitable to characterize standard parameters to evaluate fracture resistance of the material. Nevertheless, our results show that the as fabricated material undergoes notch weakening while the three post-process heat-treated materials does not undergo statistically significant notch weakening. Additionally, our results show that the values of notch tip opening at

crack nucleation are similar for the as fabricated and super-transus air-cooled specimens, while the sub-transus heat-treated and super-transus furnace-cooled specimens can exhibit notch tip openings that are over 30% greater than those of the as-fabricated specimens.

## 5. Concluding remarks

Herein, we have examined the microscale drivers and mechanisms of fracture in EBM processed Ti-6Al-4V subjected to various post-process heat-treatments using detailed in-situ fracture tests of SENT specimens. Our results show that the fracture mechanism of the as fabricated and subtransus heat-treated materials that have similar columnar prior  $\beta$ -phase grains comprising basketweave  $\alpha$ -phase and intergranular  $\alpha$ -phase microstructure is essentially the same. Both materials fracture by a single dominant crack that grows following the well-known ductile fracture mechanism involving micro-void nucleation, growth, and coalescence. The transformation of the microstructure to equiaxed prior  $\beta$ -phase grains comprising colonies of  $\alpha$ -phase lamellae and intergranular  $\alpha$ -phase following super-transus heat-treatments of the as fabricated material significantly changes the fracture mechanism. In these microstructures several microcracks of hundreds of microns in length first nucleate away from the deformed notch and then link up with the main crack that nucleates later from the deformed notch. However, the location of these microcracks in the super-transus heat-treated materials is extremely sensitive to the underlying microstructure. In the super-transus air-cooled material, the microcracks nucleate along the prior  $\beta$ -phase grain boundaries due to the extremely large plastic deformation of the grain boundary  $\alpha$ phase; while in the super-transus furnace-cooled material that comprises relatively coarser microstructural features than the air-cooled material, microcracks nucleate along the boundaries of two colonies of  $\alpha$ -phase lamellae within prior  $\beta$ -phase grains due to preferential localization of deformation in one of the colonies across a colony-colony boundary. In both the super-transus heat-treated materials, the crack growth also involves micro-void nucleation, growth, and coalescence, but this mechanism appears to be secondary and only assists in linking of microcracks with the main crack.

# Acknowledgements

The financial support provided by the Haythornthwaite Foundation through the ASME/AMD – Haythornthwaite Research Initiation Grant and the U.S. National Science Foundation grant CMMI-1944496 are gratefully acknowledged.

### References

- Al-Bermani, S. S., Blackmore, M. L., Zhang, W. & Todd, I. 2010. The Origin of Microstructural Diversity, Texture, and Mechanical Properties in Electron Beam Melted Ti-6Al-4V. *Metallurgical and Materials Transactions A*, 41, 3422-3434.
- Antonysamy, A. A., Meyer, J. & Prangnell, P. B. 2013. Effect of build geometry on the β-grain structure and texture in additive manufacture of Ti6Al4V by selective electron beam melting. *Materials Characterization*, 84, 153-168.
- ASTM:E112-13 2013. Standard Test Methods for Determining Average Grain Size. West Conshohocken, PA, USA: ASTM International.
- Blaber, J., Adair, B. & Antoniou, A. 2015. Ncorr: Open-Source 2D Digital Image Correlation Matlab Software. *Experimental Mechanics*, 55, 1105-1122.
- Book, T. A. & Sangid, M. D. 2016. Strain localization in Ti-6Al-4V Widmanstätten microstructures produced by additive manufacturing. *Materials Characterization*, 122, 104-112.
- BS:8571 2018 Method of Test for Determination of Fracture Toughness in Metallic Materials Using Single Edge Notched Tension (SENT) Specimens. London, UK: British Standards Institution.
- Cunningham, R., Nicolas, A., Madsen, J., Fodran, E., Anagnostou, E., Sangid, M. D. & Rollett, A. D. 2017. Analyzing the effects of powder and post-processing on porosity and properties of electron beam melted Ti-6Al-4V. *Materials Research Letters*, 5, 516-525.
- Cvijović-Alagić, I., Gubeljak, N., Rakin, M., Cvijović, Z. & Gerić, K. 2014. Microstructural morphology effects on fracture resistance and crack tip strain distribution in Ti–6Al–4V alloy for orthopedic implants. *Materials & Design*, 53, 870-880.
- Dang, N., Liu, L., Adrien, J., Cazottes, S., Xiao, W., Ma, C., Zhou, L. & Maire, E. 2019. Crack nucleation and growth in α/β titanium alloy with lamellar microstructure under uniaxial tension: 3D X-ray tomography analysis. *Materials Science and Engineering: A*, 747, 154-160.
- de Formanoir, C., Michotte, S., Rigo, O., Germain, L. & Godet, S. 2016. Electron beam melted Ti–6Al–4V: Microstructure, texture and mechanical behavior of the as-built and heat-treated material. *Materials Science and Engineering: A*, 652, 105-119.
- Draelos, L., Nandwana, P. & Srivastava, A. 2020. Implications of post-processing induced microstructural changes on the deformation and fracture response of additively manufactured Ti–6Al–4V. *Materials Science and Engineering: A*, 139986.

- Facchini, L., Magalini, E., Robotti, P. & Molinari, A. 2009. Microstructure and mechanical properties of Ti-6Al-4V produced by electron beam melting of pre-alloyed powders. *Rapid Prototyping Journal*, 15, 171-178.
- Frazier, W. E. 2014. Metal Additive Manufacturing: A Review. *Journal of Materials Engineering and Performance*, 23, 1917-1928.
- Galarraga, H., Lados, D. A., Dehoff, R. R., Kirka, M. M. & Nandwana, P. 2016. Effects of the microstructure and porosity on properties of Ti-6Al-4V ELI alloy fabricated by electron beam melting (EBM). *Additive Manufacturing*, 10, 47-57.
- Galarraga, H., Warren, R. J., Lados, D. A., Dehoff, R. R., Kirka, M. M. & Nandwana, P. 2017. Effects of heat treatments on microstructure and properties of Ti-6Al-4V ELI alloy fabricated by electron beam melting (EBM). *Materials Science and Engineering: A*, 685, 417-428.
- Gross, A. J. & Ravi-Chandar, K. 2017. On the deformation and failure of Al 6061-T6 in plane strain tension evaluated through in situ microscopy. *International Journal of Fracture*, 208, 27-52.
- Han, Q., Kang, Y., Hodgson, P. D. & Stanford, N. 2013. Quantitative measurement of strain partitioning and slip systems in a dual-phase steel. *Scripta Materialia*, 69, 13-16.
- Herzog, D., Seyda, V., Wycisk, E. & Emmelmann, C. 2016. Additive manufacturing of metals. *Acta Materialia*, 117, 371-392.
- Jha, J. S., Toppo, S. P., Singh, R., Tewari, A. & Mishra, S. K. 2021. Deformation behavior of Ti-6Al-4V microstructures under uniaxial loading: Equiaxed Vs. transformed-β microstructures. *Materials Characterization*, 171.
- Kang, J., Ososkov, Y., Embury, J. D. & Wilkinson, D. S. 2007. Digital image correlation studies for microscopic strain distribution and damage in dual phase steels. *Scripta Materialia*, 56, 999-1002.
- Kok, Y., Tan, X. P., Wang, P., Nai, M. L. S., Loh, N. H., Liu, E. & Tor, S. B. 2018. Anisotropy and heterogeneity of microstructure and mechanical properties in metal additive manufacturing: A critical review. *Materials & Design*, 139, 565-586.
- Liu, S. & Shin, Y. C. 2019. Additive manufacturing of Ti6Al4V alloy: A review. *Materials & Design*, 164.
- Liu, Z., Zhao, Z., Liu, J., Wang, Q., Guo, Z., Zeng, Y., Yang, G. & Gong, S. 2021. Effects of the crystallographic and spatial orientation of α lamellae on the anisotropic in-situ tensile behaviors of additive manufactured Ti–6Al–4V. *Journal of Alloys and Compounds*, 850, 156886.
- Lutjering, G. & Williams, J. C. 2007. Titanium, Springer Science & Business Media.
- Marteau, J., Haddadi, H. & Bouvier, S. 2013. Investigation of strain heterogeneities between grains in ferritic and ferritic-martensitic steels. *Experimental Mechanics*, 53, 427-439.
- Murr, L. E., Gaytan, S. M., Ramirez, D. A., Martinez, E., Hernandez, J., Amato, K. N., Shindo, P. W., Medina, F. R. & Wicker, R. B. 2012. Metal Fabrication by Additive Manufacturing Using Laser and Electron Beam Melting Technologies. *Journal of Materials Science & Technology*, 28, 1-14.
- Murr, L. E., Quinones, S. A., Gaytan, S. M., Lopez, M. I., Rodela, A., Martinez, E. Y., Hernandez, D. H., Martinez, E., Medina, F. & Wicker, R. B. 2009. Microstructure and mechanical behavior of Ti–6Al–4V produced by rapid-layer manufacturing, for biomedical applications. *Journal of the Mechanical Behavior of Biomedical Materials*, 2, 20-32.

- Nandwana, P., Lee, Y., Ranger, C., Rollett, A. D., Dehoff, R. R. & Babu, S. S. 2019. Post-processing to Modify the α Phase Micro-Texture and β Phase Grain Morphology in Ti-6Al-4V Fabricated by Powder Bed Electron Beam Melting. *Metallurgical and Materials Transactions A*, 50, 3429-3439.
- Ososkov, Y., Wilkinson, D. S., Jain, M. & Simpson, T. 2007. In-situ measurement of local strain partitioning in a commercial dual-phase steel. *International Journal of Materials Research*, 98, 664-673.
- Raisson, G. & Samarov, V. Sponsor Org.:. HIP of complex shape parts keys to development and industrial manufacturing. 1996-12-31 1996 United States. Research Org.:: ASM International, Materials Park, OH (United States).
- Ren, Y. M., Lin, X., Fu, X., Tan, H., Chen, J. & Huang, W. D. 2017. Microstructure and deformation behavior of Ti-6Al-4V alloy by high-power laser solid forming. *Acta Materialia*, 132, 82-95.
- Tammas-Williams, S., Zhao, H., Léonard, F., Derguti, F., Todd, I. & Prangnell, P. B. 2015. XCT analysis of the influence of melt strategies on defect population in Ti–6Al–4V components manufactured by Selective Electron Beam Melting. *Materials Characterization*, 102, 47-61.
- Tasan, C. C., Hoefnagels, J. P. M., Diehl, M., Yan, D., Roters, F. & Raabe, D. 2014. Strain localization and damage in dual phase steels investigated by coupled in-situ deformation experiments and crystal plasticity simulations. *International Journal of Plasticity*, 63, 198-210.
- Zhai, Y., Galarraga, H. & Lados, D. A. 2015. Microstructure Evolution, Tensile Properties, and Fatigue Damage Mechanisms in Ti-6Al-4V Alloys Fabricated by Two Additive Manufacturing Techniques. *Procedia Engineering*, 114, 658-666.
- Zhao, X., Li, S., Zhang, M., Liu, Y., Sercombe, T. B., Wang, S., Hao, Y., Yang, R. & Murr, L. E. 2016. Comparison of the microstructures and mechanical properties of Ti–6Al–4V fabricated by selective laser melting and electron beam melting. *Materials & Design*, 95, 21-31.
- Zheng, X., Ghassemi-Armaki, H. & Srivastava, A. 2020. Structural and microstructural influence on deformation and fracture of dual-phase steels. *Materials Science and Engineering: A*, 138924.